JACS
JOURNAL OF THE AMERICAN CHEMICAL SOCIETY
Article
pubs.acs.org/JACS

A General Chelate-Assisted Co-Assembly to Metallic Nanoparticles-Incorporated Ordered Mesoporous Carbon Catalysts for Fischer–Tropsch Synthesis

Zhenkun Sun,[†,‡,§] Bo Sun,[†,§] Minghua Qiao,[†] Jing Wei,[†] Qin Yue,[†] Chun Wang,[†] Yonghui Deng,*[,†] Serge Kaliaguine,[‡] and Dongyuan Zhao*[,†]

[†]Department of Chemistry and Shanghai Key Lab of Molecular Catalysis and Innovative Materials, Advanced Materials Laboratory, Fudan University, Shanghai 200433, P. R. China

[‡]Department of Chemical Engineering, Laval University, Quebec, QC, G1V 0A6, Canada

Ⓢ *Supporting Information*

ABSTRACT: The organization of different nano objects with tunable sizes, morphologies, and functions into integrated nanostructures is critical to the development of novel nanosystems that display high performances in sensing, catalysis, and so on. Herein, using acetylacetone as a chelating agent, phenolic resol as a carbon source, metal nitrates as metal sources, and amphiphilic copolymers as a template, we demonstrate a chelate-assisted multicomponent coassembly method to synthesize ordered mesoporous carbon with uniform metal-containing nanoparticles. The obtained nanocomposites have a 2-D hexagonally arranged pore structure, uniform pore size (~4.0 nm), high surface area (~500 m^2/g), moderate pore volume (~0.30 cm^3/g), uniform and highly dispersed Fe_2O_3 nanoparticles, and constant Fe_2O_3 contents around 10 wt %. By adjusting acetylacetone amount, the size of Fe_2O_3 nanoparticles is readily tunable from 8.3 to 22.1 nm. More importantly, it is found that the metal-containing nanoparticles are partially embedded in the carbon framework with the remaining part exposed in the mesopore channels. This unique semiexposure structure not only provides an excellent confinement effect and exposed surface for catalysis but also helps to tightly trap the nanoparticles and prevent aggregating during catalysis. Fischer–Tropsch synthesis results show that as the size of iron nanoparticles decreases, the mesoporous Fe–carbon nanocomposites exhibit significantly improved catalytic performances with C_{5+} selectivity up to 68%, much better than any reported promoter-free Fe-based catalysts due to the unique semiexposure morphology of metal-containing nanoparticles confined in the mesoporous carbon matrix.

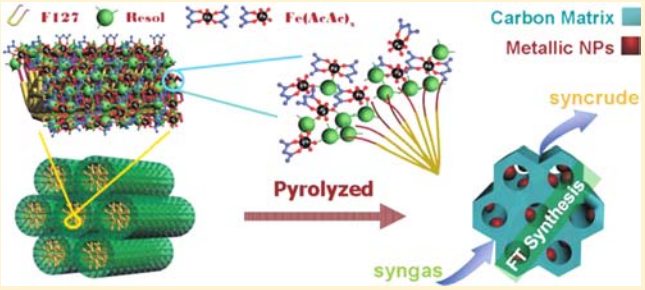

1. INTRODUCTION

The diverse utilization of fossil energies combined with a high-efficiency catalytic process has received renewed interest because of the worldwide demand for a decreased dependence on petroleum.[1] Significant advances in coal gasification technology for syngas (a mixture of CO and H_2) production foresee Fischer–Tropsch synthesis (FTS) as a major contender on the energy scene since it is a key step in which syngas can be catalytically converted to liquid, clean fuels, and chemical feedstocks via surface polymerization reaction.[2] FTS has been proved to be catalyzed by certain transition metals, with Co, Fe, and Ru presenting the highest activity.[3] As it is a heterogeneous catalytic process, the size of the active phase is one of the most important factors determining the catalytic performance of the FTS.[4−7] The particle size effect of Fe- and Co-based catalysts has been extensively investigated, and it has been demonstrated that both activity and selectivity in FTS are strongly affected by their size.[1,8−10] Therefore, exploring effective methods to control the nucleation and growth of supported metallic particles and eventually to design size-variable catalysts is crucial for development of high-performance FTS catalysts in industry.[4,8,11]

In FTS, Fe-based catalysts have recently attracted ever-growing attention because they are relatively cost-efficient and have high water–gas shift (WGS) activity which helps to make up deficit of H_2 in the syngas from modern energy-efficient coal or biomass gasifiers.[12−14] The syngas derived from biomass usually contains large amounts of CO_2 (30 vol % from gasification). For the Co- or Ru-based catalysts, purification of syngas by removing CO_2 is necessary before use to avoid dilution of H_2 and CO and a decrease in catalyst activity and C_{5+} selectivity.[15] Conversely, the removal of CO_2 from the raw syngas is not needed as CO_2 can also be hydrogenated by Fe-based catalyst, thus reducing the cost involved in the CO_2 separation step.[16] It has been demonstrated that the intermediate phase of iron carbides is essential to obtain a high FTS performance.[17−19] As a result, iron catalysts

Received: July 20, 2012
Published: September 28, 2012

designedly supported on carbon materials, such as activated carbon,[4] carbon microspheres,[20] or nanotubes,[21,22] have been widely investigated in FTS with an aim to directly introduce carbide intermediate phases by using these supports as carbon sources and thus to increase the activity and desirable long-chain hydrocarbon selectivity.[17−19,23] In this regards, the impregnation method has been frequently used to deposit iron species onto carbon supports. Although the obtained catalysts have a higher catalytic activity, they usually exhibit low selectivity to desired products or a high deactivation rate due to the gradual migration and agglomeration of active phases during the reaction.[24−26] As a kind of novel carbon nanomaterials, ordered mesoporous carbons have been demonstrated as excellent catalytic supports due to their uniform and tunable pore size (2.0 − 50 nm), regularly aligned pore architecture, high surface area (up to 2500 m^2/g), large pore volume, and good electrical conductivity and thermal stability.[27,28] Undoubtedly, the integration of ordered mesoporous carbons with iron nanoparticles holds great promise in developing iron-based catalysts with highly accessible active sites that are stably confined in the carbon matrix.[29−31]

Several reports have shown that ordered mesoporous carbons with incorporated functional nanoparticles can be synthesized through either a hard-templating approach using presynthesized ordered mesoporous silica as a template[5,27] or soft-templating approach based on the coassembly of triblock copolymers Pluronic F127 and resol (a soluble phenolic resin precursor) or resorcinol-formaldehyde (RF) in the presence of metal salts.[32−39] However, due to the lack of effective control over the synthesis, the nanoparticles in the above-reported nanomaterials either suffer severe aggregation with broad size distributions or are less controllable. Additionally, by directly employing presynthesized inorganic nanoparticles as a metallic precursor,[40,41] a variety of mesoporous carbons with embedded metal (oxides) nanoparticles have reported. This strategy requires well-dispersed uniform nanoparticles that are usually stabilized by capping agents to prevent agglomeration. However, the capped nanoparticles can not be well dispersed in the solution of carbon precursors and templates, which makes the entirety synthesis less controllable. Herein, we demonstrate, for the first time, a chelate-assisted coassembly route for the synthesis of high-quality ordered mesoporous carbons incorporated with highly dispersed uniform Fe_2O_3 nanoparticles for application in FTS. The synthesis is based on a multiconstituent coassembly process which is accomplished by slow evaporation of an ethanol solution containing soluble resol as a carbon source, iron nitrate as a metallic precursor, acetylacetone (acac) as a chelating agent, and Pluronic F127 as a template. The obtained nanocomposites have a 2-D hexagonally arranged pore structure, uniform pore size (~4.0 nm), high surface area (~500 m^2/g), moderate pore volume (~0.30 cm^3/g), uniform and highly dispersed Fe_2O_3 nanoparticles with readily controllable size in the range of 8.3−22.1 nm, and constant Fe_2O_3 contents around 10 wt %. It is moreover found that the Fe_2O_3 nanoparticles are partially embedded in the carbon framework with the remaining part exposed in the mesopore channels. This unique semiexposure structure not only provides an excellent confinement effect and exposed surface for catalysis but also helps to tightly trap the nanoparticles and prevent aggregating during catalysis. After being reduced by hydrogen, the obtained Fe-based mesoporous carbon catalyst shows remarkable high selectivity (~ 68%) to C_{5+} products and stability in the FTS reaction, which is due to the unique semiexposure nanostructure and high porosity of the catalysts. As the size of the supported Fe-based nanoparticles decrease, the resultant catalysts show significantly enhanced performance with higher conversion of carbon monoxide, lower selectivity of methane, and higher selectivity toward C_{5+} hydrocarbons.

2. EXPERIMENTAL SECTION

2.1. Chemicals. Poly(ethylene oxide)-*block*-poly(propylene oxide)-*block*-poly-(ethylene oxide) triblock copolymer Pluronic F127 (M_w = 12 600, $PEO_{106}PPO_{70}PEO_{106}$) was purchased from Acros Corp. $Fe(NO_3)_3{\cdot}9H_2O$ and $Co(NO_3)_2{\cdot}6H_2O$, phenol, formalin solution (37 wt %), sodium hydroxide, hydrochloric acid, ethanol, and acetylacetone were purchased from Shanghai Chemical Corp. All chemicals were used as received without any further purification. Millipore water was used in all experiments.

2.2. Preparation of Mesoporous Carbon Composites. Soluble resol precursors were prepared by using phenol and formaldehyde in a base-catalyzed process according to the procedure reported previously.[42] The detailed synthesis procedure is available in the Supporting Information. The metallic nanoparticle-supporting mesoporous carbon composites were synthesized through the chelate-assisted multicomponent coassembly pathway. Typically, 1.0 g of Pluronic F127 was dissolved in 14.0 g of absolute ethanol. Then, 5.0 g of the resol precursor solution (20 wt % in ethanol) was added and stirred for 10 min. Into the above mixture, 0.2 g of $Fe(NO_3)_3{\cdot}9H_2O$ or 0.15 g of $Co(NO_3)_2{\cdot}6H_2O$ (0.5 mmol) dissolved in 3.0 g of ethanol was dropped. Subsequently, a certain amount of acac (0, 0.01, 0.03, or 0.09 g; 0−45 wt % relative to the hydrated metal nitrite) was added. After further stirring for 30 min, the mixture was cast onto Petri dishes, followed by evaporation of ethanol for 8 h at room temperature in a hood. The resulting sticky films were subjected to thermocuring at 100 °C for 24 h. The obtained composite films were scrapped off and ground into powders, followed by pyrolysis in a tube furnace at 600 °C for 3 h under N_2 atmosphere to decompose the triblock copolymer templates, carbonize the resol precursors, and *in situ* generate metal or metal-oxide nanocrystallites. Before heating, the tube furnace was purged with N_2 gas for at least 1 h to remove air. The temperature ramp rate was 1 °C min^{-1}. A series of samples with similar Fe-contents were synthesized and designated as M−C-*z*, wherein, M and *z* refer to the corresponding metallic species and the grain size (nm) of metal-containing nanoparticles, respectively.

2.3. Fischer−Tropsch Synthesis. Prior to the FTS reaction, the Fe−C-*z* samples (1.0 g) diluted with quartz powder was reduced *in situ* in 5% H_2/Ar (50 mL/min) for 16 h at 400 °C (ramping rate: 2 °C/min). Catalytic tests were conducted at H_2/CO of 2 or 1 (volume ratio), flow rate of 15 mL/min, 270 °C, and 2.0 MPa in a tubular fixed-bed reactor (i.d. = 10 mm). Product analysis was performed on line with two gas chromatographs.

2.4. Measurements and Characterizations. Small-angle X-ray scattering (SAXS) measurements were taken on a Nanostar U SAXS system (Bruker, Germany) using Cu K_α radiation (40 kV, 35 mA). The *d*-spacing values were calculated by the formula $d = 2\pi/q$, and the unit cell parameters were calculated with the formula $a = 2d_{10}/\sqrt{3}$. Nitrogen sorption−desorption isotherms were measured at 77 K with a Micromeritcs Tristar 3000 analyzer (U.S.A.). Before measurements, the samples were degassed in a vacuum at 200 °C for 10 h. The Brunauer−Emmett−Teller (BET) method was utilized to calculate the specific surface areas (S_{BET}) using adsorption data in a relative pressure range from 0.05 to 0.25. By using the Barrett−Joyner−Halenda (BJH) model, the pore volumes and size distributions were derived from the adsorption branches of isotherms, and the total pore volumes (V_t) were estimated from the adsorbed amount at a relative pressure P/P_0 of 0.995. Powder X-ray diffraction (XRD) patterns were recorded on a Bruker D4 X-ray diffractometer (Germany) with Ni-filtered Cu K_α radiation (40 kV, 40 mA). Transmission electron microscopy (TEM) measurements were conducted on a JEM-2100 microscope (JEOL, Japan) operated at 200 kV. Samples were first dispersed in ethanol and then collected using carbon-film-covered copper grids for analysis. The

FTS product analysis was performed online with two gas chromatographs. A TDX-01 packed column connected to a thermal conductivity detector (TCD) was used to analyze H_2, N_2, CO, CH_4, and CO_2, while hydrocarbons (C_1−C_{30}) were analyzed with a PONA capillary column connected to a flame ionization detector (FID). The hydrocarbon selectivities were calculated on carbon basis. Thermogravimetric analysis (TGA) curves were carried out using a Mettler Toledo TGA-SDTA851 analyzer (Switzerland) from 25 to 900 °C in an air flow of 80 mL/min at a heating rate of 5 °C/min.

3. RESULTS AND DISCUSSION

3.1. Synthesis of Metallic Nanoparticles Incorporated Mesoporous Carbon Composites (M−C-*z*). Ordered mesoporous carbon materials with embedded Fe-nanoparticles can be synthesized through an innovative chelate-assisted coassembly strategy. The synthesis was accomplished by a slow evaporation of an ethanol solution containing ferric nitrate, acetylacetone, resol, and Pluronic F127. After the evaporation, a mesostructured iron-oxides/resol/F127 composite film was obtained, which was subjected to thermosetting and further pyrolysis to remove the F127 template and carbonize the phenolic resin. By adjusting the amount of acac (0−45 wt % relative to metal source), ordered mesoporous carbons incorporated with varisized metallic nanoparticles could be obtained.

SAXS patterns of the Fe−C-*z* samples show three well-resolved scattering peaks at *q* values of around 0.60, 1.10, and 1.13 nm^{-1}, respectively, which can be exactly indexed to the 10, 11, and 20 reflections of a 2-D hexagonal mesostructure (space group *p*6 mm) (Figure 1a). The cell parameters of the resultant samples are calculated to be ∼11.0 nm (Table 1). The structural regularity deteriorates slightly as the acac amount decreases from 45 wt % (0.09 g) for the sample Fe−C-8 to 0 wt % (0 g) for Fe−C-22, indicating that an appropriate amount of acac is favorable to retain the ordered mesostructure in this system. Further increase of acac amount to even 90 wt % (0.18 g) was found to have no significant influence on the mesostructure ordering, suggesting a good tolerance toward organic additives of the synthesis. Wide-angle XRD patterns (Figure 1b) of the Fe−C-*z* samples display six resolved diffraction peaks, which can be assigned to the 220, 311, 400, 422, 511, and 440 reflections of the maghemite phase (γ-Fe_2O_3) (JCPDS card number 89-5892). This result indicates that the iron-oxide nanoparticles are well crystallized in the carbon matrix. Calculation based on the Debye−Scherrer equation reveals that the crystalline sizes of the Fe_2O_3 nanoparticles are ∼8.3, 11.9, 19.3, and 22.1 nm for Fe−C-8, -12, -19 and -22 samples, respectively (Table 1). Fe−C-8 sample was further carbonized at 800 °C for 3 h under N_2 atmosphere to check the influence of temperature on the type of iron-based particles. The wide-angle XRD patterns (Figure S8) showed that the well-resolved diffraction peaks can be assigned to mixed phases of α-Fe_2O_3, γ- Fe_2O_3, Fe, and Fe_3C or Fe_2C.

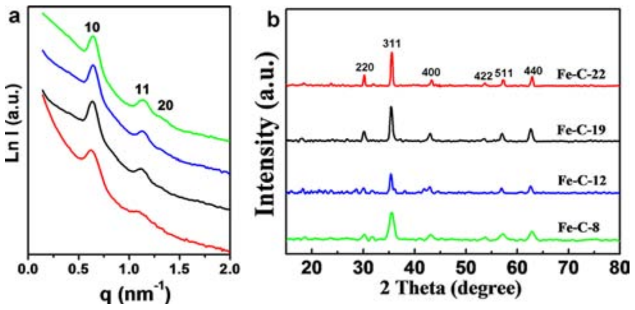

Figure 1. SAXS (a) and wide-angle XRD patterns (b) of the iron-oxide nanoparticles incorporated ordered mesoporous carbon nanocomposites synthesized with different amount of acac. (i) Fe−C-8, (ii) Fe−C-12, (iii) Fe−C-19, and (iv) Fe−C-22 samples, respectively.

TEM images of all Fe−C-*z* nanocomposites show stripe-like and hexagonally arranged pore morphology over large domains, confirming an ordered mesostructure with 2-D hexagonal pore symmetry (Figure 2a−d). As can be seen in the TEM image of the sample Fe−C-8 (Figure 2a), uniform Fe_2O_3 nanoparticles are highly dispersed in the carbon matrix. The size distribution curve displays a mean diameter centered at ∼8 nm with a standard deviation of about 10% (Figure 2a, inset). When the acac dosage is decreased to 15 wt % (0.03 g; respect to metal source) for the sample Fe−C-12, Fe_2O_3 nanoparticles of about 12 nm can be obtained without aggregation (Figure 2b). Further decrease of acac amount from 5 wt % (0.01 g) for the sample Fe−C-19 to 0 wt % for Fe−C-22 leads to much larger nanoparticles, and even some of them are about 19−23 nm in size (Figure 2c,d). With the enlargement of the particle size, these iron-oxide nanoparticles can penetrate the carbon walls and get stuck in two and even three mesopores but are still confined in the carbon matrix. These results reveal that the acac chelating agent plays an important role in regulating the growth of iron oxides, which makes it convenient to tune their particle sizes by simply varying acac amount.

Table 1. Structural and Textural Properties of the Metallic Nanoparticles-Incorporated Ordered Mesoporous Carbon Prepared with Various Conditions

sample	a_0,[a] nm	S_{BET},[b] m^2g^{-1}	S_{mic},[c] m^2g^{-1}	V_v,[d] cm^3g^{-1}	V_{mic},[e] m^3g^{-1}	D_p,[f] nm	D_c,[g] nm	W_T,[h] nm	M_xO_y,[i] (wt %)
Fe−C-8	11.3	545	330	0.33	0.15	4.3	8.3	7.0	9.87
Fe−C-12	11.5	513	317	0.30	0.14	4.3	11.9	7.2	9.91
Fe−C-19	11.3	492	306	0.30	0.14	4.2	19.3	7.1	9.75
Fe−C-22	11.3	501	311	0.29	0.14	3.8	22.1	7.5	10.0
Co−C-8	11.1	558	314	0.51	0.14	3.8	7.8	7.3	13.2
Co−C-11	10.6	511	261	0.51	0.12	3.8	11.0	6.8	15.2
Co−C-14	10.8	514	309	0.40	0.14	3.4	14.5	7.4	14.6

[a] Cell parameters calculated from SAXS patterns. [b] BET specific surface areas evaluated in P/P_0 from 0.05 to 0.25. [c] Micropore surface areas calculated through the *t*-plot method. [d] Total pore volumes estimated based on the volume adsorbed at P/P_0 of ∼0.995. [e] Micropore volumes calculated through the *t*-plot method. [f] Pore sizes derived from the adsorption branches of the isotherms by using the BJH method. [g] Average crystal size estimated by the Scherrer equation from XRD patterns and TEM images for the samples Fe−C-*z* and Co−C-*z*, respectively. [h] Wall thickness (W_T) values calculated from $W_T = a_0 - D_p$, where a_0 is the cell parameter and D_p is the mesopore diameter. [i] Metal-oxide weight percentage obtained by combusting the carbon components (Figures S1 and S5).

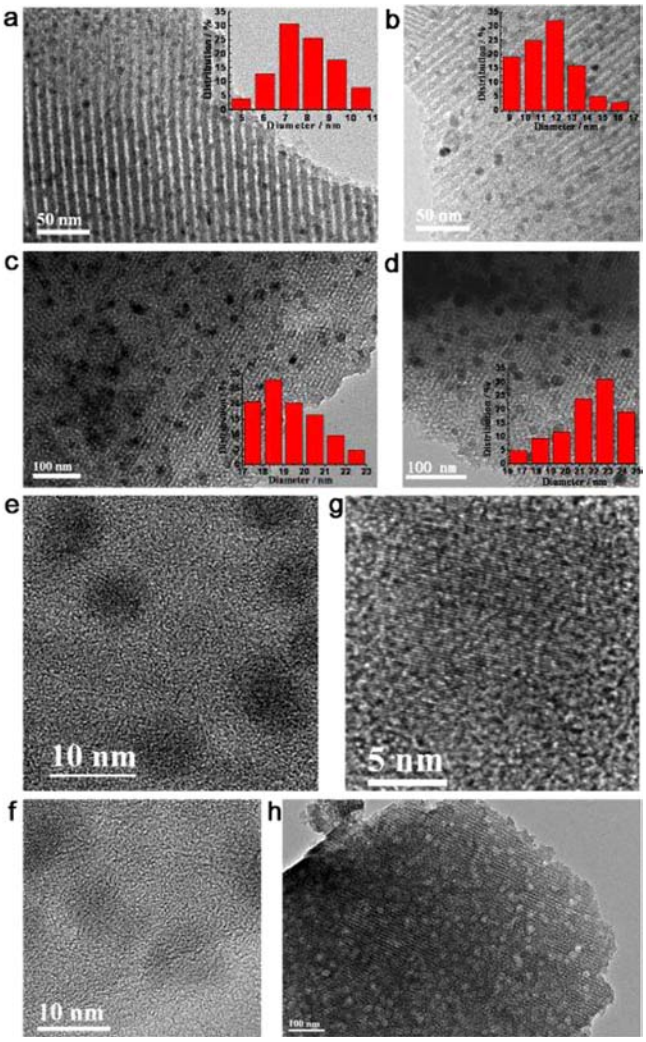

Figure 2. TEM images of the iron-oxide nanoparticles-incorporated ordered mesoporous carbon nanocomposites (Fe–C-*z*) synthesized with different amount of acac. (a,e) Fe–C-8, (b,f) Fe–C-12, (c) Fe–C-19, and (d,g) Fe–C-22. (h) TEM image of the sample obtained by treating Fe–C-22 with HCl solution, showing uniform nanopores, confirming the embedment of iron-oxide nanoparticles in the carbon wall. Insets in (a–d) are the corresponding particle size distributions of the iron-oxide nanoparticles in the samples Fe–C-8, -12, -19, and -22, respectively.

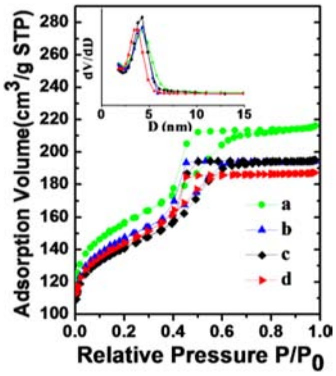

Figure 3. N_2 adsorption–desorption isotherms and the corresponding pore size distributions (inset) of the Fe_2O_3 nanoparticles incorporated ordered mesoporous carbon nanocomposites (Fe–C-*z*) synthesized by using different amount of acac, (a) Fe–C-8, (b) Fe–C-12, (c) Fe–C-19, and (d) Fe–C-22, respectively.

High-resolution TEM (HRTEM) images (Figure 2e–g) clearly show that the well-crystallized Fe_2O_3 nanoparticles are embedded in the amorphous carbon matrix with a homogeneous dispersion. Furthermore, close observation of TEM images shows that the iron-oxide nanoparticles in the obtained composites have unique semiexposure morphology, with one part of the nanoparticle being partially exposed to pore channels and the other part being tightly trapped in the carbon framework (Figure 2e). To further get insight into the nanoparticle location in the carbon matrix, the Fe_2O_3 particles were removed from the sample Fe–C-22 by soaking in a diluted HCl solution, and plentiful honeycomb-like nanopores were left (Figure 2h). This clearly confirms that Fe_2O_3 nanoparticles are effectively incorporated in the carbon framework.

N_2 sorption–desorption isotherms (Figure 3) of all the Fe–C-*z* samples show representative type-IV curves with pronounced H_2 hysteresis loops and large uptake at a low relative pressure. It is attributed to the existence of well-developed meso- and microporosity formed by the removal of F127 template and burn-out of C, H, and O from the phenolic resin framework during pyrolysis at 600 °C.[35] These results suggest that the obtained Fe–C-*z* samples possess similar pore structures and features. The pore size distribution curves derived from adsorption branches using BJH model reveal the presence of relatively uniform mesopores in all samples (Table 1 and Figure 3 inset). The mean mesopore sizes of the Fe–C-*z* samples range from 3.8–4.3 nm, slightly declining with the decrease of acac amount. The calculated values of pore wall thicknesses are in the range of 7.0–7.5 nm, less than the sizes (8–22 nm) of Fe_2O_3 particles as mentioned above. Consequently, it is reasonable to deduce that these Fe_2O_3 particles partially penetrate into the mesopore walls and are partially exposed in the mesopore channels, which is also evidenced by the HRTEM observations (Figure 2e). The BET surface areas and pore volumes of the mesoporous nanoparticle/carbon composites are in the range of 500–545 m^2/g and 0.29–0.33 cm^3/g, respectively (Table 1). TGA indicates that all the Fe–C-*z* samples have a similar Fe_2O_3 content (~10.0 wt %) due to the same added amount of the iron source (Table 1 and Figure S1). To further confirm that the iron-based nanoparticles are rooted in the pore walls, the porous carbon sample was prepared by removing iron-based nanoparticles from Fe–C-22 sample. The N_2 sorption–desorption isotherms of the obtained porous carbon show two adsorption steps associated with hysteresis loops, indicative a bimodal of mesoporosity (Figure S9). The new broad plateau around 25 nm in the pore size distribution profile proves that nanoparticles were removed, leaving pores of around 25 nm in the mesoporous carbon.

By utilization of the similar effective complexation between acac and Co^{2+} ions, a series of size-tunable Co-based nanoparticles-incorporated mesoporous carbon nanocomposites can be synthesized by using the constant ratio of cobalt nitrate as a metallic source and different amounts of acac. By varying acac ratio, the size of the cobalt-oxide nanocrystals is readily adjusted into 7.8, 11.0, and 14.5 nm for the samples Co–C-8, -11, and -14, without causing noticeable aggregation and changing the mesostructure (Figure 4). Compared with the Fe–C-*z* samples, the metallic nanoparticles in the Co–C-*z* samples are slightly smaller (Table 1, more detailed results in

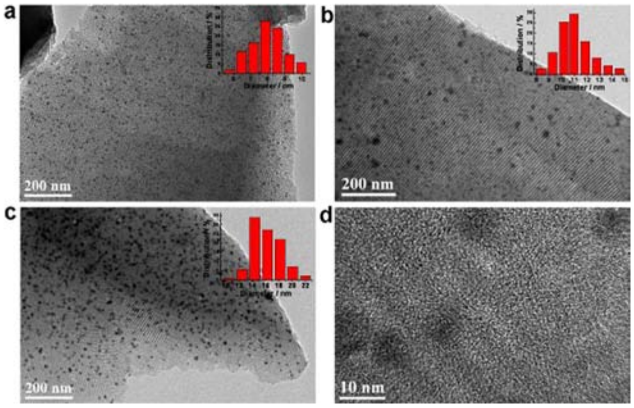

Figure 4. TEM images of the cobalt-oxide nanoparticles incorporated ordered mesoporous carbon nanocomposites (Co−C-*z*) synthesized by using different amount of acac: (a) Co−C-8, (b) Co−C-11, and (c) Co−C-14, respectively. (d) HRTEM images of the sample Co−C-8 showing a typical semiexposed morphology. Insets in (a−c) are Co-based particle size distributions of sample Co−C-8, -11, and -14, respectively.

Figures S2−S5). Specifically, TEM images of the sample Co−C-8 confirmed that cobalt-oxide nanoparticles with uniform size were highly dispersed in the ordered mesoporous carbon matrix (Figure S4). HRTEM images showed that the cobalt-oxide nanoparticles were homogeneously embedded in the mesoporous carbon frameworks and partially exposed to the pore channels (Figure S4 inset), which was similar to the Fe−C-*z* samples.

The formation of the oxide nanoparticles with the semiexposed morphology in the ordered mesoporous composites is mainly attributed to the chelating effect of acac molecules. High dosage of acac chelate agent can help to restrain the crystal growth through effectively coordinating iron (or cobalt) species, retarding their hydrolysis during the coassembly process and even preventing the aggregation during pyrolysis. Taking the Fe−C-*z* sample as an example (Scheme 1), in an ethanol solution containing F127 template, resol, and Fe^{3+} ions, the resol molecules with several phenolic hydroxyl groups serve as a bridge which not only interact with the EO segments of Pluronic F127 template via hydrogen bonding[35] but also coordinate with Fe^{3+} ions forming a dark-blue ferric iron−phenol complexes (Figure S6). Meanwhile, the Fe^{3+} ions are partially chelated by acac molecules due to the strong complexation. After casting on a substrate, the solution was concentrated upon continuous evaporation of ethanol, the amphiphilic F127 macromolecules associated with resol and Fe^{3+} ions spontaneously assemble into a highly ordered mesostructure. In this mesostructure, $Fe(acac)_x$ complexes are homogeneously "dissolved" in the resol matrix that surrounds the hexagonally arranged F127 micelles. After thermosetting at 100 °C, the ordered mesoporous composite is consolidated, with the $Fe(acac)_x$ complex being well retained in the phenolic resin domain due to the high melting point of $Fe(acac)_x$ (180 °C).[43] During pyrolysis at 600 °C in N_2, the F127 template molecules are first decomposed, leaving highly ordered aligned mesopores, and the phenolic resin is then carbonized into a rigid carbon framework accompanied with an *in situ* growth of γ-Fe_2O_3 nanoparticles via a slow decomposition of $Fe(acac)_x$ complexes, resulting in iron-oxide nanoparticles incorporated mesoporous carbons. Without the addition of acac molecules, the iron species in the phenolic resin can readily migrate, aggregate, and grow during both thermosetting and pyrolysis treatments because of the low melting points of ferric nitrate (47 °C), leading to the formation of large particles up to 22.1 nm. With acac added, the nanoclusters of iron oxides formed at the early stage of pyrolysis can be capped with acac molecules which prevent them from fast growth. Therefore, with an appropriate amount of acac, the iron oxides can grow from the carbon matrix (i.e., the pore walls) and penetrate into the pore channels, resulting in a unique semiexposed morphology. Incorporation of smaller nanoparticles in the mesostructured composites using higher acac amount is favorable to homogeneous carbonization of frameworks compared to the case of larger nanoparticles systems (e.g., Fe−C-22), and mesoporous carbons with better regularity of pore arrangement can be obtained. However, when the acac content is higher than 45 wt %, the iron-oxide particles show no significant change in the particle size because of the limitation of acac chelating capacity (Figure S7).

Scheme 1. Illustration of the Chelate-Assisted Co-Assembly Route for the Synthesis of Ordered Mesoporous Carbon Nanocomposites Incorporated with Size-Tunable Metallic Nanoparticles[a]

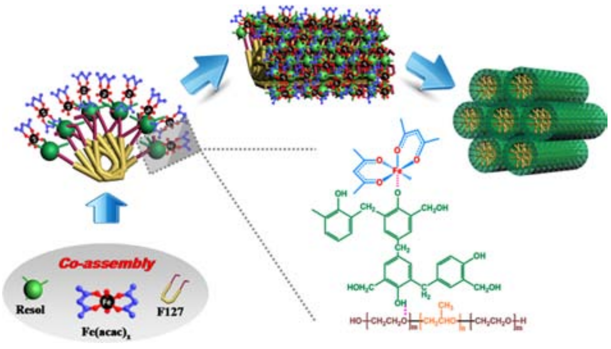

[a]The resol molecule with several phenolic hydroxyl groups serves as a bridge which not only interacts with the EO segments of Pluronic F127 template via hydrogen bonding but also coordinates with Fe^{3+} ions forming ferric iron−phenol complexes. Meanwhile, the Fe^{3+} ions can be partially chelated by ligand acac molecules.

As acac molecules can coordinate with various metal ions to form stable chelate complexes,[44−46] this simple but versatile chelate-assisted coassembly method can be used as guidance for the design of mesoporous carbon composites incorporated with transition-metal-based nanoparticles for various applications. It is believed that the unique semiexposure configuration of the nanoparticles in our mesoporous nanocomposites is beneficial to catalysis.[3,5,47] First, the exposed surface can make the Fe_2O_3 nanoparticles in good contact with reactants (substrates) within pore channels with less diffusion restriction. Second, the partial incorporation in carbon walls provides the nanoparticles with enough protection, preventing them from leaching, sintering, and aggregating. Third, numerous pore channels of the stable mesoporous carbons can serve as nanoreactors for efficient reactions. Consequently, it is expected that the unique nanostructure of the nanocomposites M−C-*z* hold a great promise for applications in electronics, electrochemistry, and catalysis.

3.2. Fischer−Tropsch Synthesis of Fe−C-*z* Mesoporous Carbon Composites. Four mesoporous Fe-carbon composites, Fe−C-8, -12, -19, and -22 with Fe-based nanocrystals of 8.3−22.1 nm, were studied as catalysts in

FTS under industrially relevant conditions (H_2/CO = 2, 20 bar, 270 °C) which have been widely used in previous reports.[4,10,18,19] Before the reaction, the catalysts were *in situ* reduced in 5% H_2/Ar at 400 °C and activated according to the process reported previously.[18,19] The F–T synthesis results are summarized in Table 2 and Figure 5. It is found that when the nanoparticle size increases from 8 nm (for the sample Fe–C-8) to ~19 nm (Fe–C-12), the CO conversion shows a gradual decrease from 90.1 to 73.5%. For Fe–C-22 catalyst with the largest Fe-based particles (about 22 nm), the CO conversion drops sharply to 37.8%. As shown in Figure 5a, a methane selectivity of ~30% and a C_{5+} selectivity of ~25% can be observed on the Fe–C-22 catalyst, which are typical for promoter-free Fe-based catalysts under the identical reaction conditions.[19] Obviously, as the nanoparticle size decreases, the methane selectivity decreases and the C_{5+} yield increases monotonically. Notably, among these catalysts, the Fe–C-8 catalyst exhibits the best catalysis performance with the lowest methane selectivity of only 13.4% and the highest C_{5+} yield of 60%. To our knowledge, this result is the best one among all promoter-free Fe-based catalysts previously reported, including the Fe-in-CNT, Fe-out-CNT, and Fe-activated carbon catalysts.[18,22,48] The normalized activity per gram of Fe for the sample Fe–C-8 is also comparable to those of the Fe-based catalysts reported previously (Table S1). As Fe-based F–T catalysts have higher water–gas shift activity which helps to make up deficit of H_2 in the syngas, we decrease the H_2/CO ratio to 1 to evaluate the performance of Fe–C-8 catalyst. The results indicate that the methane selectivity decreases further to 8.2%, while C_{5+} selectivity increases to 68% (Table 2). Additionally, a significant change in the catalytic performance with the nanoparticle size is observed for selectivities to olefins and paraffins as summarized in Table 2 and Figure 5b. It can be clearly seen that the mesoporous Fe–C-*z* catalysts with smaller Fe_2O_3 nanoparticles show higher olefin to paraffin molar ratio. Since the loading of Fe species is similar for all catalysts investigated, the particle size effect is considered as the dominant factor affecting the catalytic performance. The lower selectivity to methane and the higher one for C_{5+} hydrocarbons of the catalysts with smaller Fe-based nanoparticles indicates a higher abundance of active sites for the C–C coupling rather than for hydrogenation of atomic C to methane. The selectivity toward olefins is also consistent with the lowered hydrogenation activity of the catalyst with smaller Fe-based nanoparticles.

Table 2. Comparison of the Catalytic Performance of the Iron-Based Nanoparticles Incorporated Ordered Mesoporous Carbon Catalysts

		hydrocarbon selectivity[c] (%)				
catalysts	CO conversion (%)	CH_4	C_{5-12}	C_{12+}	CO_2 selectivity (%)	$C_=/C_n$[d]
Fe–C-22[a]	37.8	30.4	20.1	4.6	27.4	0.8
Fe–C-19[a]	73.5	21.4	27.9	5.5	26.8	0.9
Fe–C-12[a]	84.4	16.5	36.8	6.2	21.5	1.1
Fe–C-8[a]	90.1	13.4	43.2	16.9	13.3	1.5
Fe–C-8[b]	74.7	8.2	48.8	19.2	25.1	1.7

[a] Reaction condition: T = 270 °C, P = 2.0 MPa, H_2/CO = 2, $W_{Fe/F(H_2+CO)}$ = 2.5 g·h/mol, TOS = 24 h. [b] Reaction condition: T = 270 °C, P = 2.0 MPa, H_2/CO = 1, $W_{Fe/F(H_2+CO)}$ = 2.5 g·h/mol, TOS = 24 h. [c] Hydrocarbon selectivity has been normalized with the exception of CO_2. [d] $C_=/C_n$ is the molar ratio of olefin to paraffin with C_{2-4}.

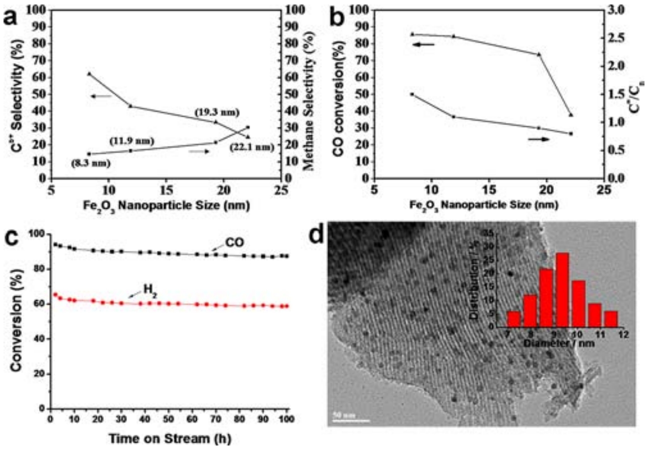

Figure 5. Catalytic performances of the iron-based nanoparticles incorporated ordered mesoporous carbon (Fe–C-*z*) in FTS. (a) Plots of C_{5+} selectivity and methane yield as a function of Fe_2O_3 particle size. (b) Plots of CO conversion and olefin/paraffin ratio as a function of Fe_2O_3 particle size. (c) Conversions of CO and H_2 vs reaction time over a period of 100 h on stream. (d) TEM image of the used catalyst Fe–C-8, indicating that the nanoparticles remain a high dispersibility and excellent stability against sintering.

Figure 5c presents the F–T reaction performance over 100 h on the reduced Fe–C-8 catalyst. The CO conversion is ~94% initially and then decreases insignificantly to 88% after 70 h on stream, with no further change over prolonged reaction time, clearly revealing an excellent stability. By varying the H_2/CO ratio to 1, the mesoporous Fe–C-8 catalyst still exhibits excellent stability over 100 h reaction (Figure 6). For comparison, CO conversion on the carbon nanotubes-supported iron catalyst was found to drop much faster (from 45 to 15%) within 50 h of testing, even at a reaction temperature (50 °C) lower than the present case.[21] TEM characterizations of the used catalysts shows that the particle size of iron species is only around 10 nm after running for 100 h (Figure 5d). The negligible enlargement of the Fe-based nanoparticle size can be attributed to embedding the particles

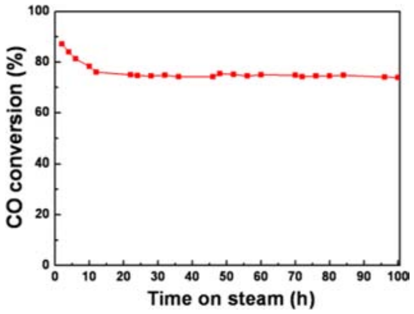

Figure 6. Conversions of CO vs reaction time of the catalyst Fe–C-8 over a period of 100 h on stream (H_2/CO = 1). The CO conversion is ~88% initially and then decreases insignificantly to 75% after 13 h on stream, with no further change over prolonged reaction time.

in the mesoporous carbon matrix and confinement effect, which effectively prevents the migration and sintering of the nanoparticles during the F−T reaction.

4. CONCLUSIONS

We have demonstrated a facile chelate-assisted multicomponent coassembly to synthesize ordered mesoporous carbons with embedded and highly dispersed metal-oxide nanoparticles as novel catalysts for Fischer−Tropsch synthesis. By utilization of the capability of the chelating agent acac in restraining the fast growth of nanoparticles in the carbon matrix, metal-oxide nanoparticles that are trapped in the carbon matrix and partially exposed to the pore channels have been created. Using ferric nitrate as the metal source, a series of iron-oxide nanoparticles incorporated ordered mesoporous carbon (Fe−C-*z*) materials have been obtained by adjusting acac amounts. Owing to the high porosity of the carbon matrix and the unique semiexposed structure of iron-oxide nanoparticles, the mesoporous Fe/carbon nanocomposite catalyst (Fe−C-8) with a small Fe-particle size (~8 nm) shows an excellent catalytic performance with a remarkable stability and C_{5+} selectivity (>68%) in FTS. It is believed that this chelate-assisted coassembly can be used as a general synthetic method for designing various function-integrated nanostructures containing incorporated functional nanoparticles for diverse applications.

■ ASSOCIATED CONTENT

Ⓢ Supporting Information

TEM images, TGA curves of Fe−C-*z*, wide-angle XRD patterns, TGA curve, SAXS patterns, TEM images, N_2 sorption isotherms and pore size distributions of Co−C-*z*, photograph of the as-made Fe−C-*z* composite film, comparison data of the activity and selectivity of the reduced Fe−C-8 catalyst. This material is available free of charge via the Internet at http://pubs.acs.org.

■ AUTHOR INFORMATION

Corresponding Author

dyzhao@fudan.edu.cn; yhdeng@fudan.edu.cn

Author Contributions

§These authors contributed equally.

Notes

The authors declare no competing financial interest.

■ ACKNOWLEDGMENTS

This work was supported by NSF of China (20890123, 20821140537, 21073043 and 21073040), State Key 973 Program of PRC (2012CB224805), Shanghai Leading Academic Discipline Project (B108), and Science & Technology Commission of Shanghai Municipality (08DZ2270500, 10jc1401800), the program of New Century Excellent Talents (NCET-08-0126), the Innovation Program of Shanghai Municipal Education Commission (13ZZ004), Shanghai Rising Star Project of STCSM (12QH1400300) and the National Basic Research Program of China (2012CB224804). D.Y.Z. also thanks the support from TOTAL Cor.

■ REFERENCES

(1) Kang, J. C.; Zhang, S. L.; Zhang, Q. H.; Wang, Y. *Angew. Chem., Int. Ed.* **2009**, *48*, 2565.

(2) Ertl, G.; Knözinger, H.; Schüth, F.; Weitkamp, J. In *Handbook of Heterogeneous Catalysis*; Wiley-VCH: Weinheim, Germany, 2008; Vol. 6.

(3) MartInez, A.; Lopez, C.; Marquez, F.; Diaz, I. *J. Catal.* **2003**, *220*, 486.

(4) Jones, V. K.; Neubauer, L. R.; Bartholomew, C. H. *J. Phys. Chem.* **1986**, *90*, 4832.

(5) Lu, A. H.; Nitz, J. J.; Comotti, M.; Weidenthaler, C.; Schlichte, K.; Lehmann, C. W.; Terasaki, O.; Schuth, F. *J. Am. Chem. Soc.* **2010**, *132*, 14152.

(6) Boudart, M.; McDonald, M. A. *J. Phys. Chem.* **1984**, *88*, 2185.

(7) den Breejen, J. P.; Sietsma, J. R. A.; Friedrich, H.; Bitter, J. H.; de Jong, K. P. *J. Catal.* **2010**, *270*, 146.

(8) Bezemer, G. L.; Bitter, J. H.; Kuipers, H. P. C. E.; Oosterbeek, H.; Holewijn, J. E.; Xu, X.; Kapteijn, F.; van Dillen, A. J.; de Jong, K. P. *J. Am. Chem. Soc.* **2006**, *128*, 3956.

(9) Xiao, C. X.; Cai, Z. P.; Wang, T.; Kou, Y.; Yan, N. *Angew. Chem., Int. Ed.* **2008**, *47*, 746.

(10) Dong, H. H.; Xie, M.; Xu, J.; Li, M.; Peng, L.; Guo, X.; Ding, W. *Chem. Commun.* **2011**, *47*, 4019.

(11) Mahajan, D.; Gütlich, P.; Ensling, J.; Pandya, K.; Stumm, U.; Vijayaraghavan, P. *Energy Fuels* **2003**, *17*, 1210.

(12) Jin, Y. M.; Datye, A. K. *J. Catal.* **2000**, *196*, 8.

(13) Gideon, B. F. *Appl. Catal., A* **2007**, *328*, 237.

(14) van Steen, E.; Claeys, M. *Chem. Eng. Technol.* **2008**, *31*, 655.

(15) Hamelinck, C. N.; Faaij, A. P. C.; den Uil, H.; Boerrigter, H. *Energy* **2004**, *29*, 1743.

(16) Abelló, S.; Montané, D. *ChemSusChem* **2011**, *4*, 1538.

(17) Raupp, G. B.; Delgass, W. N. *J. Catal.* **1979**, *58*, 348.

(18) Chen, W.; Fan, Z. L.; Pan, X. L.; Bao, X. H. *J. Am. Chem. Soc.* **2008**, *130*, 9414.

(19) Yu, G. B.; Sun, B.; Pei, Y.; Xie, S.; Yan, S.; Qiao, M. H.; Fan, K. N.; Zhang, X.; Zong, B. *J. Am. Chem. Soc.* **2009**, *132*, 935.

(20) Xiong, H. F.; Moyo, M.; Motchelaho, M. A. M.; Jewell, L. L.; Coville, N. J. *Appl. Catal., A* **2010**, *388*, 168.

(21) van Steen, E.; Prinsloo, F. F. *Catal. Today* **2002**, *71*, 327.

(22) Guczi, L.; Stefler, G.; Geszti, O.; Koppany, Z.; Konya, Z.; Molnar, E.; Urban, M.; Kiricsi, I. *J. Catal.* **2006**, *244*, 24.

(23) Jung, H.; Thomson, W. J. *J. Catal.* **1992**, *134*, 654.

(24) de Jong, K. P. *Oil Gas Sci. Technol.* **2006**, *61*, 527.

(25) Torres Galvis, H. M.; Bitter, J. H.; Khare, C. B.; Ruitenbeek, M.; Dugulan, A. I.; de Jong, K. P. *Science* **2012**, *335*, 835.

(26) Chen, W.; Pan, X. L.; Willinger, M. G.; Su, D. S.; Bao, X. H. *J. Am. Chem. Soc.* **2006**, *128*, 3136.

(27) Joo, S. H.; Choi, S. J.; Oh, I.; Kwak, J.; Liu, Z.; Terasaki, O.; Ryoo, R. *Nature* **2001**, *412*, 169.

(28) Deng, Y. H.; Cai, Y.; Sun, Z. K.; Gu, D.; Wei, J.; Li, W.; Guo, X. H.; Yang, J. P.; Zhao, D. Y. *Adv. Funct. Mater.* **2010**, *20*, 3658.

(29) Xiong, K.; Li, J. L.; Liew, K.; Zhan, X. D. *Appl. Catal., A* **2010**, *389*, 173.

(30) Khodakov, A. Y.; Chu, W.; Fongarland, P. *Chem. Rev.* **2007**, *107*, 1692.

(31) Lu, A. H.; Schmidt, W.; Matoussevitch, N.; Bönnemann, H.; Spliethoff, B.; Tesche, B.; Bill, E.; Kiefer, W.; Schüth, F. *Angew. Chem., Int. Ed.* **2004**, *43*, 4303.

(32) Wu, Z. X.; Webley, P. A.; Zhao, D. Y. *Langmuir* **2010**, *26*, 10277.

(33) Zhai, Y. P.; Dou, Y. Q.; Liu, X. X.; Park, S. S.; Ha, C. S.; Zhao, D. Y. *Carbon* **2010**, *49*, 545.

(34) Zhai, Y. P.; Dou, Y. Q.; Liu, X. X.; Tu, B.; Zhao, D. Y. *J. Mater. Chem.* **2009**, *19*, 3292.

(35) Gao, P.; Wang, A.; Wang, X.; Zhang, T. *Chem. Mater.* **2008**, *20*, 1881.

(36) Yao, J.; Li, L.; Song, H.; Liu, C.; Chen, X. *Carbon* **2009**, *47*, 436.

(37) Sterk, L.; Górka, J.; Jaroniec, M. *Colloids Surf., A* **2010**, *362*, 20.

(38) Wang, Y.; He, C. X.; Brouzgou, A.; Liang, Y. R.; Fu, R. W.; Wu, D. C.; Tsiakaras, P.; Song, S. Q. *J. Power Sources* **2012**, *200*, 8.

(39) Li, J.; Gu, J.; Li, H.; Liang, Y.; Hao, Y.; Sun, X.; Wang, L. *Microporous Mesoporous Mater.* **2010**, *128*, 144.

(40) Górka, J.; Jaroniec, M. *J. Phys. Chem. C* **2008**, *112*, 11657.

(41) Choma, J.; Jedynak, K.; Marszewski, M.; Jaroniec, M. *Appl. Surf. Sci.* **2012**, *258*, 3763.

(42) Meng, Y.; Gu, D.; Zhang, F. Q.; Shi, Y. F.; Yang, H. F.; Li, Z.; Yu, C. Z.; Tu, B.; Zhao, D. Y. *Angew. Chem., Int. Ed.* **2005**, *44*, 7053.

(43) Hoene, J. V.; Charles, R. G.; Hickam, W. M. *J. Phys. Chem.* **1958**, *62*, 1098.

(44) Tollan, C.; Echeberria, J.; Marcilla, R.; Pomposo, J.; Mecerreyes, D. *J. Nanopart. Res.* **2009**, *11*, 1241.

(45) Kim, Y. T.; Park, Y. S.; Myung, H.; Chae, H. K. *Colloids Surf., A* **2008**, *313*–*314*, 260.

(46) Navio, J.; Colon, G.; Litter, M. I.; Bianco, G. N. *J. Mol. Catal. A: Chem.* **1996**, *106*, 267.

(47) Wu, Z. X.; Hao, N.; Xiao, G. K.; Liu, L. Y.; Webley, P. A.; Zhao, D. Y. *Phys. Chem. Chem. Phys.* **2011**, *13*, 2495.

(48) Jambor, J. L.; Dutrizac, J. E. *Chem. Rev.* **1998**, *98*, 2549.